Hindawi
Shock and Vibration
Volume 2021, Article ID 1787525, 17 pages
https://doi.org/10.1155/2021/1787525

Research Article

Dynamic Analysis of a Fault Planetary Gear System under Nonlinear Parameter Excitation

Jianchao Han,[1,2] Yinghui Liu,[3] Lei Liang,[1] Yang Zhao,[1] and Huibo Zhang[3]

[1]*Department of Astronautics Engineering, Harbin Institute of Technology, Harbin 150001, China*
[2]*Beijing Satellite Manufacturing Factory, Beijing 100094, China*
[3]*School of Mechanical Engineering, Hebei University of Technology, Tianjin 300401, China*

Correspondence should be addressed to Lei Liang; lianglei@hit.edu.cn

Received 29 April 2021; Revised 1 June 2021; Accepted 30 June 2021; Published 14 July 2021

Academic Editor: Siqi Bu

In order to facilitate lubrication and avoid the gear stuck due to thermal expansion, there needs to be a gap between the tooth profiles. As a strong nonlinear factor, the backlash will affect the motion state of the planetary gear system. When the gear failures occur, the motion state of the system will accordingly change. In this study, the meshing stiffness of the gear pair with tooth tip chipping fault is calculated by combining the analytic geometry method and the potential energy method. Then, a new nonlinear dynamic model including tooth backlash, time-varying mesh stiffness, and manufacturing error is established to study the dynamic response of the system. The equations of motion are derived by the Lagrangian method and solved by the numerical integration method. Taking the excitation frequency and tooth backlash as the variation parameters, respectively, the dynamic characteristics of the system are analyzed by comparing the global bifurcation diagrams between the health system and the fault system, and the path of the system into chaos is revealed. At the same time, the local characteristics of the system are revealed through the phase diagrams and Poincaré maps. The results show that with the variation of excitation frequency and tooth backlash, the fault system presents a more complex motion state. This study can provide the theoretical support for dynamic design and fault diagnosis of planetary gear transmission systems under the environment of gear fault-prone.

1. Introduction

Planetary gear systems are widely used in aerospace, agricultural machinery, construction machinery, and other fields because of their high transmission ratio and transmission efficiency [1]. For the purpose that the gears can be fully lubricated and avoid jamming, tooth backlash between the engaged teeth is indispensable. However, the backlash is a strong nonlinear factor for the dynamic characteristics of the gear system. Due to the nonlinear factors, such as backlash, gear fault, and so on, the system exhibits different motion states with the variational excitation frequency. Hence, for better dynamic design and fault diagnosis for planetary gear systems, it is necessary to analyze their dynamic characteristics.

In recent decades, many scholars have conducted modeling analyses on the gear transmission system. In 1994, Kahraman [2] proposed a dynamic model of the planetary gear system and studied the load-sharing characteristics. Later, the vibration modes of the planetary gear system [3–5] and the suppression law of the meshing phase to the planetary modal response are analyzed [6]. Then, the load distribution coefficient is deduced based on the model [7–9]. Wang et al. [10] revealed the nonlinear phenomena and evolution mechanisms of bifurcation and chaos via a three-degree-of-freedom torsional vibration model. Then, Shen et al. [11] studied the dynamic characteristics of spur gear systems using the incremental harmonic balance method. In the planetary gear system, gear errors are inevitable, such as installation errors [12], manufacturing errors [13], and

geometric errors [14], and the influence on the system is also analyzed [15].

Backlash and meshing stiffness are nonlinear factors for the gear system. To analyze the dynamic characteristics of the planetary gear system, the nonlinear dynamic model containing the tooth backlash [16–18] and time-varying meshing stiffness was established [19–22]. Then, Huang et al. [23] and Pan and Vicuña [24] introduced the fractal backlash to the model. However, under high-speed and light-load conditions, gears may appear as tooth backside contact. Therefore, a multistate dynamic model was established by Liu et al. [25], and the variation law of the meshing force under different meshing conditions was analyzed. The influence of bearing clearance [26] and gear surface modification [27] on the dynamic response of the planetary gear system was revealed. Later, a nonlinear dynamic model of the multistage gear transmission was established by Zhao and Ji [28] and Xiang et al. [29], and the nonlinear dynamic characteristics of the system are analyzed at the same time.

Due to poor lubrication, impact load, and stress concentration, gear failures often occur and the dynamic response of the system will change accordingly. For early fault detection, Shi et al. [30] analyzed the fault characteristics under variable load. Pan et al. [31] analyzed the frequency components of the vibration signal in the fault and the healthy state. Considering the flexible ring gear and bearing fault, Liu et al. [32] presented a rigid-flexible coupling planetary gear dynamic model. By establishing the meshing stiffness model under spalling fault, Luo et al. [33] and Xiang et al. [34] analyzed the dynamic characteristics of the planetary gear system. Later, Shen et al. [35] proposed a purely torsional model to analyze the dynamic characteristics of planetary gear under wear fault. Yang et al. [36] proposed a nonlinear dynamic model with tooth backlash and bearing clearance and analyzed the vibration response under crack fault [37–39]. Luo et al. [40] established the meshing stiffness model for spalling and pitting failures and compared the dynamic response under different failure types.

In the previous literature, the dynamic response of the planetary gear system under crack failure, pitting failure, and spalling was researched. However, there are limited research studies on the nonlinear dynamic characteristics of planetary gear systems with tooth tip chipping fault under nonlinear parameters excitation. Therefore, in order to reveal the dynamic characteristics of the fault system, this study established a nonlinear dynamic model containing tooth backlash, time-varying meshing stiffness, and static transmission error and analyzed the chaos and bifurcation characteristics of the system via choosing the excitation frequency and tooth backlash as variable parameters. The rest of the study is organized as follows. Section 2 establishes the planetary gear dynamic model. In Section 3, the dynamic characteristics of the system are analyzed by taking the tooth backlash and rotation speed as control variables. Finally, some conclusions are given in Section 4.

2. Dynamic Model of the Planetary Gear System

The planetary gear system has a complex structure that is different from fixed shaft gearboxes. In order to study the nonlinear dynamic behavior, a pure torsional dynamic model of the planetary gear system is proposed, which contains a sun gear s, a ring gear r, a carrier c, and N planet gears p_i ($i = 1, 2, \ldots, N$), as shown in Figure 1. In this model, all gears are standard spur gears. The carrier with planet gears fixed on is connected with the input shaft, and the sun gear is attached with the output shaft. The ring gear is fixed. In order to simplify the model, all components are assumed to be rigid.

2.1. System Excitations

2.1.1. Time-Varying Meshing Stiffness of Gears with Tooth Tip Chipping Fault. The potential energy method is a common method for calculating meshing stiffness. In the method, the gear tooth is regarded as a variable cross-section cantilever beam fixed on the tooth root, as shown in Figure 2. The total meshing stiffness can be composed of bending stiffness k_b, axial compression stiffness k_a, shear stiffness, Hertz contact stiffness k_h, and fillet foundation stiffness k_f. When in the gear occurs tooth tip chipping failure, a part of the material will fall off the tooth tip, which will affect the cross-sectional area and the moment of inertia of the tooth faulty part, as shown in Figure 3. Thereby, to estimate the meshing stiffness of gear pairs with tooth tip chipping, an accurate stiffness model is established.

In order to simplify the model, the fracture surface is simplified as a plane, as shown in Figure 3. The intersection line between the plane and the tooth profile surface is the curve L_3, and the intersection line with the gear end surface denotes the straight L_2. In the three-dimensional coordinate system, the involute tooth profile equation Ω_1 can be expressed as

$$\begin{bmatrix} x \\ y \\ z \end{bmatrix} = \begin{bmatrix} \cos(\alpha_2) & -\sin(\alpha_2) & 0 \\ \sin(\alpha_2) & \cos(\alpha_2) & 0 \\ 0 & 0 & 0 \end{bmatrix} \begin{bmatrix} u \\ v \\ w \end{bmatrix}, \tag{1}$$

where u and v represent the coordinate of the involute in the UOV coordinate system, which can be described as

$$\begin{cases} u = R_b[\sin(\theta_x + \alpha_x) - (\theta_x + \alpha_x)\cos(\theta_x + \alpha_x)], \\ v = R_b[\cos(\theta_x + \alpha_x) + (\theta_x + \alpha_x)\sin(\theta_x + \alpha_x)]. \end{cases} \tag{2}$$

In the three-dimensional coordinate system, the fracture surface equation Ω_2 can be written as

$$z = \frac{[(x - x_a)(y_a - y_b) - (x_a - x_b)(y - y_a)]}{(x_a - x_b)(y_a - y_c) + (y_a - y_b)(x_c - x_a)} z_c. \tag{3}$$

The equation of the curve L_2 can be deduced by simultaneous equations of (1) and (3). The equation of line L_3 in Figure 3(a) can be expressed as

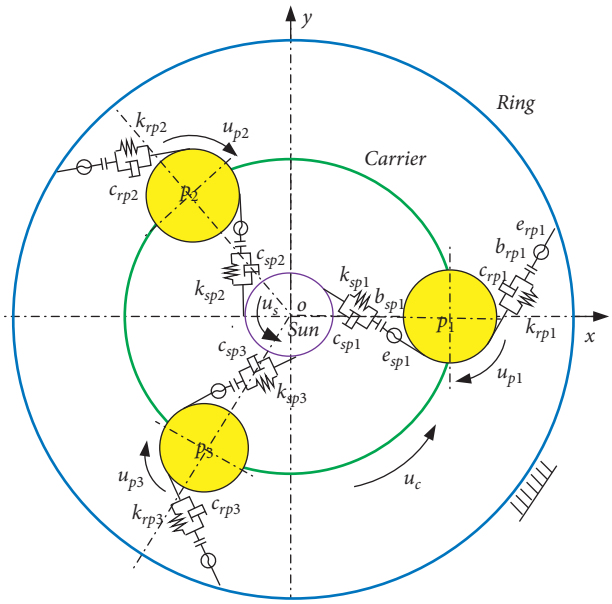

Figure 1: The dynamic model of planetary gear transmission.

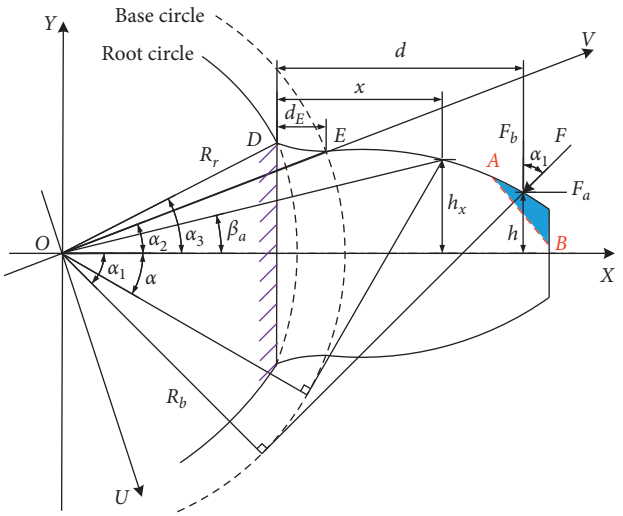

Figure 2: Cantilever beam of spur gear with tooth tip chipping.

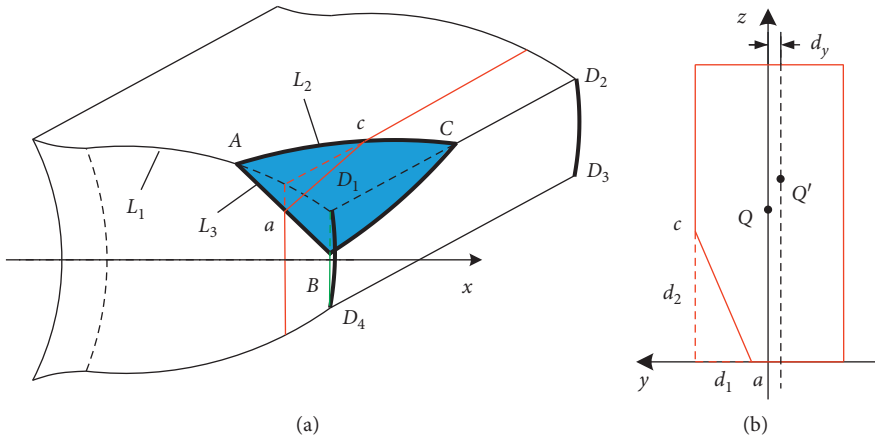

Figure 3: Diagram of the tooth tip chipping part for the tooth.

$$x = \frac{(R_b/\cos(\alpha_a))\sin(\beta_a) - x_b}{(R_b/\cos(\alpha_a))\cos(\beta_a) - (m/2)(z_e + 2h_a^*)\cos(\beta_t)}\left(y - \frac{R_b}{\cos(\alpha_a)}\cos(\beta_a)\right) + \frac{R_b}{\cos(\alpha_a)}\sin(\beta_a),$$

$$\beta_a = \frac{\pi}{2z_e} - [(\tan(\alpha_a) - \alpha_a) - (\tan(\alpha_0) - \alpha_0)], \tag{4}$$

$$\beta_t = \frac{\pi}{2z_e} - [(\tan(\alpha_t) - \alpha_t) - (\tan(\alpha_0) - \alpha_0)].$$

As tooth tip chipping failure occurs, a part of the material will fall off the tooth tip, so the cross-sectional area and moment of inertia of the faulty part will vary accordingly, which can be deduced by the following equations:

$$A_x' = 2h_xL - \frac{1}{2}d_1d_2,$$

$$I_x' = I_x - \left[\frac{d_2d_1^3}{36} + \frac{1}{2}d_1d_2\left(h_x - \frac{1}{3}d_1\right)^2\right] - \frac{[(1/2)d_1d_2(h_x - (1/3)d_1)]^2}{2h_xL - (1/2)d_1d_2},$$

$$d_1 = \left|y_{xL_1}\right| - \left|y_{xL_3}\right|,$$

$$d_2 = \left|z_{xL_2}\right|. \tag{5}$$

Thereby, the meshing stiffness can be obtained by the potential energy method [41]:

$$\frac{1}{k_a} = \int_0^d \frac{(\sin(\alpha_1))^2}{EA_x}\mathrm{d}x,$$

$$\frac{1}{k_b} = \int_0^d \frac{[(d-x)\cos(\alpha_1) - h\sin(\alpha_1)]^2}{EI_x}\mathrm{d}x,$$

$$\frac{1}{k_s} = \int_0^d \frac{1.2(\cos(\alpha_1))^2}{2GA_x}\mathrm{d}x,$$

$$k_h = \frac{\pi E(L - d_2)}{4(1 - \nu^2)},$$

$$\frac{1}{k_f} = \frac{\cos^2\alpha_1}{EL}\left\{L^*\left(\frac{u_f}{S_f}\right)^2 + M^*\left(\frac{u_f}{S_f}\right) + P^*(1 + Q^*\tan^2\alpha_1)\right\}, \tag{6}$$

where the parameters of L^*, M^*, P^*, Q^*, u_f, and S_f are given in the study by Ma et al. [42].

The total meshing stiffness of external-external mesh can be expressed as

$$k_{\mathrm{spn}} = \sum_{i=1}^{2} \frac{1}{(1/k_{h,i}) + (1/k_{b1,i}) + (1/k_{s1,i}) + (1/k_{a1,i}) + (1/k_{f1,i}) + (1/k_{b2,i}) + (1/k_{s2,i}) + (1/k_{a2,i}) + (1/k_{f2,i})}. \tag{7}$$

In this model, the internal-external mesh is assumed to be in a healthy state, and the total meshing stiffness can be deduced in the same way:

$$k_{\mathrm{rpn}} = \sum_{i=1}^{n} \frac{1}{\left(1/k_{h,i}\right)+\left(1/k_{b1,i}\right)+\left(1/k_{s1,i}\right)+\left(1/k_{a1,i}\right)+\left(1/k_{b2,i}\right)+\left(1/k_{s2,i}\right)+\left(1/k_{a2,i}\right)+\left(1/k_{f2,i}\right)}, \tag{8}$$

where n represents the number of tooth pairs engaged at the same time. The subscript 1 indicates the driving gear, and the subscript 2 represents the driven gear.

2.1.2. Manufacturing Error and Damping. In this model, the carrier is connected to the input shaft, and the meshing frequency can be expressed as

$$\omega_m = \omega_c z_r. \tag{9}$$

Assuming that the gear teeth are exactly the same, the static transmission error between the engaged gear teeth can be described as Fourier series, where the meshing frequency is the fundamental frequency. To simplify the model, merely, the fundamental frequency is taken into account, which can be expressed as [29]

$$e_{\mathrm{spn}} = e_{\mathrm{aspn}} \sin\left(\omega_m t + \phi_{\mathrm{spn}}\right), \tag{10a}$$

$$e_{\mathrm{rpn}} = e_{\mathrm{arpn}} \sin\left(\omega_m t + \phi_{\mathrm{rpn}}\right). \tag{10b}$$

The mesh damping can be expressed as

$$c_{\mathrm{spn}} = 2\xi_{\mathrm{spn}} \sqrt{\frac{k_{\mathrm{mspn}}}{\left(1/m_s\right)+\left(1/m_{pn}\right)}}, \tag{11a}$$

$$c_{\mathrm{rpn}} = 2\xi_{\mathrm{rpn}} \sqrt{\frac{k_{\mathrm{mrpn}}}{\left(1/m_r\right)+\left(1/m_{pn}\right)}}, \tag{11b}$$

where k_{mspn} and k_{mrpn} are the arithmetic mean of k_{spn} and k_{rpn}, I_j $(j = s, ce, r, pn)$ is the moment of inertia, and m_j $(j = s, c, r, pn)$ is the equivalent mass that can be calculated by the following equations:

$$\begin{aligned} I_{ce} &= I_c + N m_{pn} r_c^2, \\ m_s &= \frac{I_s}{r_s^2}, \\ m_c &= \frac{I_{ce}}{r_c^2}, \\ m_{pn} &= \frac{I_{pn}}{r_{pn}^2}. \end{aligned} \tag{12}$$

2.1.3. Gear Backlash. In order to facilitate gear lubrication and prevent the gear from jamming during the operation, there is a gap between the engaged gear teeth. The backlash can be described by a piecewise function:

$$f\left(\delta_{\mathrm{spn}}\right) = \begin{cases} \delta_{\mathrm{spn}} - b_{\mathrm{spn}}, & \delta_{\mathrm{spn}} > b_{\mathrm{spn}}, \\ 0, & \left|\delta_{\mathrm{spn}}\right| \le b_{\mathrm{spn}}, \\ \delta_{\mathrm{spn}} + b_{\mathrm{spn}}, & \delta_{\mathrm{spn}} < -b_{\mathrm{spn}}, \end{cases} \tag{13a}$$

$$f\left(\delta_{\mathrm{rpn}}\right) = \begin{cases} \delta_{\mathrm{rpn}} - b_{\mathrm{rpn}}, & \delta_{\mathrm{rpn}} > b_{\mathrm{rpn}}, \\ 0, & \left|\delta_{\mathrm{rpn}}\right| \le b_{\mathrm{rpn}}, \\ \delta_{\mathrm{rpn}} + b_{\mathrm{rpn}}, & \delta_{\mathrm{rpn}} < -b_{\mathrm{rpn}}. \end{cases} \tag{13b}$$

2.2. Dynamic Differential Equations. According to the Lagrangian equation, the differential equations of torsional vibration under the excitations can be obtained:

$$\begin{cases} I_s \ddot{\theta}_s + \sum_{n=1}^{N} r_s F_{\mathrm{spn}} = T_{\mathrm{out}}, \\ I_{pn} \ddot{\theta}_{pn} - r_{pn} F_{\mathrm{spn}} + r_{pn} F_{\mathrm{rpn}} = 0, \\ I_{ce} \ddot{\theta}_c - \sum_{n=1}^{N} r_c F_{\mathrm{spn}} - \sum_{n=1}^{N} r_c F_{\mathrm{rpn}} = -T_{\mathrm{in}}, \end{cases} \tag{14}$$

where T_{out} and T_{in} represent the output torque and the input torque, respectively. F_{spn} and F_{rpn} are adopted to describe the meshing force which can be expressed as [20]

$$F_{\mathrm{spn}} = c_{\mathrm{spn}} \dot{\delta}_{\mathrm{spn}} + k_{\mathrm{spn}} f\left(\delta_{\mathrm{spn}}\right), \tag{15a}$$

$$F_{\mathrm{rpn}} = c_{\mathrm{rpn}} \dot{\delta}_{\mathrm{rpn}} + k_{\mathrm{rpn}} f\left(\delta_{\mathrm{rpn}}\right). \tag{15b}$$

In order to reduce the dimension of the differential equations, generalized coordinates are introduced as follows:

$$\delta_{\mathrm{spn}} = r_s \theta_s - r_{pn} \theta_{pn} - r_c \theta_c - e_{\mathrm{spn}}, \tag{16a}$$

$$\delta_{\mathrm{rpn}} = r_{pn} \theta_{pn} - r_r \theta_r - r_c \theta_c - e_{\mathrm{rpn}}. \tag{16b}$$

Due to the large numerical difference between the various nonlinear parameters, the solving progress is difficult to conduct. In order to facilitate the solution and improve the calculation efficiency, the dimensionless processing is carried out. By introducing the time scale ω_n and displacement scale b_c, the dimensionless parameters can be obtained. The dimensionless time displacement, velocity, and acceleration can be expressed as

$$\begin{aligned}
\tau &= \omega_n * t,\\
\overline{\delta}_{\mathrm{spn}} &= \frac{\delta_{\mathrm{spn}}}{b_c},\\
\dot{\overline{\delta}}_{\mathrm{spn}} &= \frac{\delta_{\mathrm{spn}}}{b_c\omega_n},\\
\ddot{\overline{\delta}}_{\mathrm{spn}} &= \frac{\ddot{\overline{\delta}}_{\mathrm{spn}}}{b_c\omega_n^2},\\
\overline{\delta}_{\mathrm{rpn}} &= \frac{\delta_{\mathrm{rpn}}}{b_c},\\
\dot{\overline{\delta}}_{\mathrm{rpn}} &= \frac{\delta_{\mathrm{rpn}}}{b_c\omega_n},\\
\ddot{\overline{\delta}}_{\mathrm{rpn}} &= \frac{\ddot{\overline{\delta}}_{\mathrm{rpn}}}{b_c\omega_n^2},\\
\omega_n &= \sqrt{\frac{k_{\mathrm{mrpn}}}{(1/m_s)+(1/m_c)}}.
\end{aligned} \tag{17}$$

The dimensionless mesh stiffness, static transmission error, and backlash are expressed as

$$\overline{e}_{\mathrm{spn}} = \frac{e_{\mathrm{aspn}}}{b_c}\sin\left(\frac{\omega_m}{\omega_n}t + \psi_{\mathrm{spn}}\right), \tag{18a}$$

$$\overline{e}_{\mathrm{rpn}} = \frac{e_{\mathrm{arpn}}}{b_c}\sin\left(\frac{\omega_m}{\omega_n}t + \psi_{\mathrm{spn}}\right), \tag{18b}$$

$$f\left(\overline{\delta}_{\mathrm{spn}}\right) = \begin{cases} \overline{\delta}_{\mathrm{spn}} - \dfrac{b_{\mathrm{spn}}}{b_c}, & \overline{\delta}_{\mathrm{spn}} > \dfrac{b_{\mathrm{spn}}}{b_c},\\ 0, & \left|\overline{\delta}_{\mathrm{spn}}\right| \le \dfrac{b_{\mathrm{spn}}}{b_c},\\ \overline{\delta}_{\mathrm{spn}} + \dfrac{b_{\mathrm{spn}}}{b_c}, & \overline{\delta}_{\mathrm{spn}} < -\dfrac{b_{\mathrm{spn}}}{b_c}, \end{cases} \tag{19a}$$

$$f\left(\overline{\delta}_{\mathrm{rpn}}\right) = \begin{cases} \overline{\delta}_{\mathrm{rpn}} - \dfrac{b_{\mathrm{rpn}}}{b_c}, & \overline{\delta}_{\mathrm{rpn}} > \dfrac{b_{\mathrm{rpn}}}{b_c},\\ 0, & \left|\overline{\delta}_{\mathrm{rpn}}\right| \le \dfrac{b_{\mathrm{rpn}}}{b_c},\\ \overline{\delta}_{\mathrm{rpn}} + \dfrac{b_{\mathrm{rpn}}}{b_c}, & \overline{\delta}_{\mathrm{rpn}} < \dfrac{-b_{\mathrm{rpn}}}{b_c}. \end{cases} \tag{19b}$$

By substituting equations (15a)–(19b) into equation (14), the differential equation of dimensionless parameters can be obtained as follows:

$$\begin{cases}
\ddot{\overline{\delta}}_{\mathrm{spn}} + \left(\dfrac{1}{m_s}+\dfrac{1}{m_c}\right)\dfrac{1}{\omega_n}\displaystyle\sum_{n=1}^{N} c_{\mathrm{spn}}\dot{\overline{\delta}}_{\mathrm{spn}} + \left(\dfrac{1}{m_s}+\dfrac{1}{m_c}\right)\dfrac{1}{\omega_n^2}\sum_{n=1}^{N}\overline{k}_{\mathrm{spn}} f\left(\overline{\delta}_{\mathrm{spn}}\right) +\\
\dfrac{1}{m_{pn}}\dfrac{1}{\omega_n}c_{\mathrm{spn}}\dot{\overline{\delta}}_{\mathrm{spn}} - \dfrac{1}{m_{pn}}\dfrac{1}{\omega_n}c_{\mathrm{rpn}}\dot{\overline{\delta}}_{\mathrm{rpn}} - \dfrac{1}{m_c}\dfrac{1}{\omega_n}\displaystyle\sum_{n=1}^{N} c_{\mathrm{rpn}}\dot{\overline{\delta}}_{\mathrm{rpn}} +\\
\dfrac{1}{m_c}\dfrac{1}{\omega_n^2}\displaystyle\sum_{n=1}^{N}\overline{k}_{\mathrm{rpn}} f\left(\overline{\delta}_{\mathrm{spn}}\right) = \dfrac{T_{\mathrm{out}} r_s}{I_s b_c \omega_n^2} + \dfrac{T_{\mathrm{in}} r_c}{I_c b_c \omega_n^2} + \dfrac{e_{\mathrm{aspn}}}{\mathrm{b_c}}\left(\dfrac{\omega_m}{\omega_n}\right)^2 \sin\left(\dfrac{\omega_m}{\omega_n}t + \psi_{\mathrm{spn}}\right),\\
\ddot{\overline{\delta}}_{\mathrm{rpn}} - \dfrac{1}{m_{pn}}\dfrac{1}{\omega_n}c_{\mathrm{spn}}\dot{\overline{\delta}}_{\mathrm{spn}} - \dfrac{1}{m_{pn}}\dfrac{1}{\omega_n^2}\overline{k}_{\mathrm{spn}} f\left(\overline{\delta}_{\mathrm{spn}}\right) + \dfrac{1}{m_{pn}}\dfrac{1}{\omega_n}c_{\mathrm{rpn}}\dot{\overline{\delta}}_{\mathrm{rpn}} + \dfrac{1}{m_c}\dfrac{1}{\omega_n^2}\overline{k}_{\mathrm{rpn}} f\left(\dot{\overline{\delta}}_{\mathrm{rpn}}\right) +\\
\dfrac{1}{m_c}\dfrac{1}{\omega_n}\displaystyle\sum_{n=1}^{N} c_{\mathrm{spn}}\dot{\overline{\delta}}_{\mathrm{spn}} + \dfrac{1}{m_c}\dfrac{1}{\omega_n^2}\sum_{n=1}^{N}\overline{k}_{\mathrm{spn}} f\left(\overline{\delta}_{\mathrm{spn}}\right) + \dfrac{1}{m_c}\dfrac{1}{\omega_n}c_{\mathrm{rpn}}\dot{\overline{\delta}}_{\mathrm{rpn}} +\\
\dfrac{1}{m_c}\dfrac{1}{\omega_n^2}\displaystyle\sum_{n=1}^{N}\overline{k}_{\mathrm{spn}} f\left(\overline{\delta}_{\mathrm{spn}}\right) = \dfrac{T_{\mathrm{in}} r_c}{I_c b_c \omega_n^2} - \dfrac{e_{\mathrm{arpn}}}{b_c}\left(\dfrac{\omega_m}{\omega_n}\right)^2 \sin\left(\dfrac{\omega_m}{\omega_n}t + \psi_{\mathrm{spn}}\right).
\end{cases} \tag{20}$$

3. Numerical Simulation and Results Analysis

Since the relative displacement between the engaged teeth has the same law, the dimensionless relative displacement of the engaged teeth between the sun gear and the planet gear is taken as the object to analyze, and the fourth-order Runge–Kutta method is used to solve the dynamics differential equations. The basic parameters of each component in the

model are given in Table 1, and the meshing parameters are given in Table 2. The displacement scale b_c is $1e-5$ m. The input torque is 100 Nm, and the transmission ratio is 4. The α_a is assigned a value of 25°, y_b is 0 mm, and z_c is 20 mm. The meshing stiffness of external-external mesh and internal-external mesh is shown in Figures 4 and 5. To avoid the influence of transient response, the first 500 response cycles of the system are omitted.

3.1. Bifurcation and Chaos of Fault and Health Systems with Excitation Frequency. The motion state of the system will convert with the variation of the excitation frequency. Therefore, the dimensionless excitation frequency Ω is chosen as the variable parameter, and the dimensionless backlash b is assigned the value of 2; the bifurcation diagram of the system in both health and fault conditions is shown in Figures 6 and 7. The largest Lyapunov exponent diagram of the health system is shown in Figure 8. As can be seen from figures, both the health and fault systems have rich chaotic and bifurcation characteristics. For the health system, when the excitation frequency Ω is between 0 and 0.69, the system presents a single-period motion and the corresponding largest Lyapunov exponent is less than zero. When it is between 0.69 and 1.28, the system undergoes a single-period motion to evolve into chaotic motion with small amplitude. When the excitation frequency changes in the range of 1.28–1.48, the system basically keeps cyclical movement, in which the largest Lyapunov exponent is less than zero. Then, the system enters the chaotic motion eventually. For the fault system, it is similar to the state of motion experienced by the health system, but in the excitation frequency range corresponding to the periodic motion of the health system, the fault system shows obvious multiple periodic motions, as shown in Figure 9. Under different tooth backlashes, the bifurcation diagram of the system is displayed in Figure 10. It can be seen that the amplitude of chaotic motion augments with the increase of the initial backlash. The system enters the chaotic motion earlier as the speed increases if the backlash is designed large.

In order to further analyze the local characteristics of the health system and fault system, phase diagrams and Poincaré maps are used to describe the local characteristics of the system. Figures 11–15 are the phase diagram and Poincaré maps of the two systems at different excitation frequencies. It can be seen from Figure 11 that the health system exhibits a single-period motion at $\Omega = 0.5$, while the fault system exhibits a multiple period motion. When Ω equals to 1, as shown in Figure 12, both of the two systems are in chaotic motion. When Ω is 1.34, as shown in Figure 13, the health system exhibits single-period motion, while the fault system presents multiple periodic motions. When Ω is 4, as shown in Figure 14, the health system exhibits quasiperiodic motion, while the faulty system appears as small amplitude chaotic motion. As Ω continues to increase, the health system exhibits the single-periodic motion at $\Omega = 1.47$, while the faulty system occurs in chaotic motion, as shown in Figure 15. Hence, when the health system exhibits periodic motion, the fault system exhibits the multiperiod or pseudoperiodic motion at the corresponding excitation frequency.

Table 1: Parameters of the dynamic model.

Parameter name	Sun gear	Ring gear	Planet gear	The carrier
Number of parts	1	1	3	1
Number of teeth	19	57	19	—
Gear module (mm)	3.2	3.2	3.2	—
Pressure angle (°)	20	20	20	—
Inertia moment (kg·m^2)	$3.85E-04$	$2.4E-02$	$3.85E-04$	$4.93E-03$

Table 2: Meshing parameters.

Parameter name	Sun-planet	Ring-planet
Damping ratio	0.07	0.07
Error amplitude (m)	$1e-5$	$1e-5$

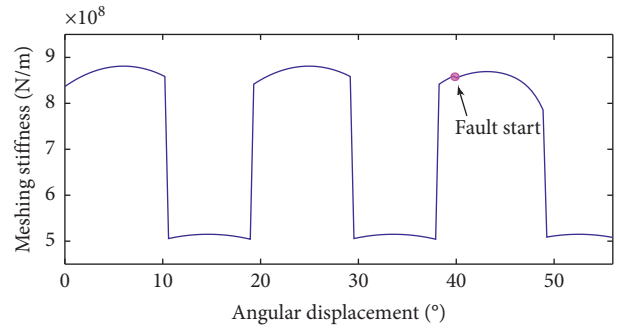

Figure 4: Meshing stiffness of external-external mesh.

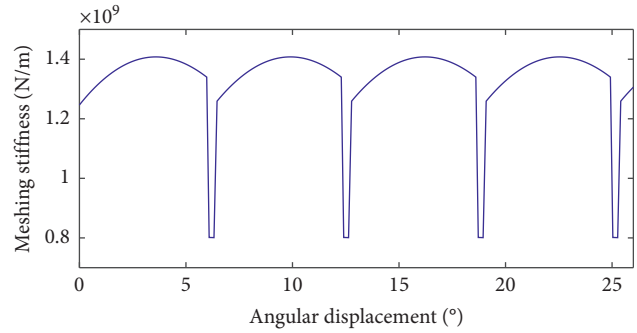

Figure 5: Meshing stiffness of internal-external mesh.

3.2. Bifurcation and Chaos of Fault and Health Systems with Different Initial Backlashes. In order to facilitate lubrication, there needs to be a gap between the engaged gear teeth and the value of the initial backlash that will affect the dynamic characteristics of the gear system. Therefore, the dimensionless backlash b is chosen as the variable parameter to study the dynamic characteristics of the system with the dimensionless excitation frequency Ω to be 1.6. When the backlash varies between 0 and 3, the bifurcation diagrams of

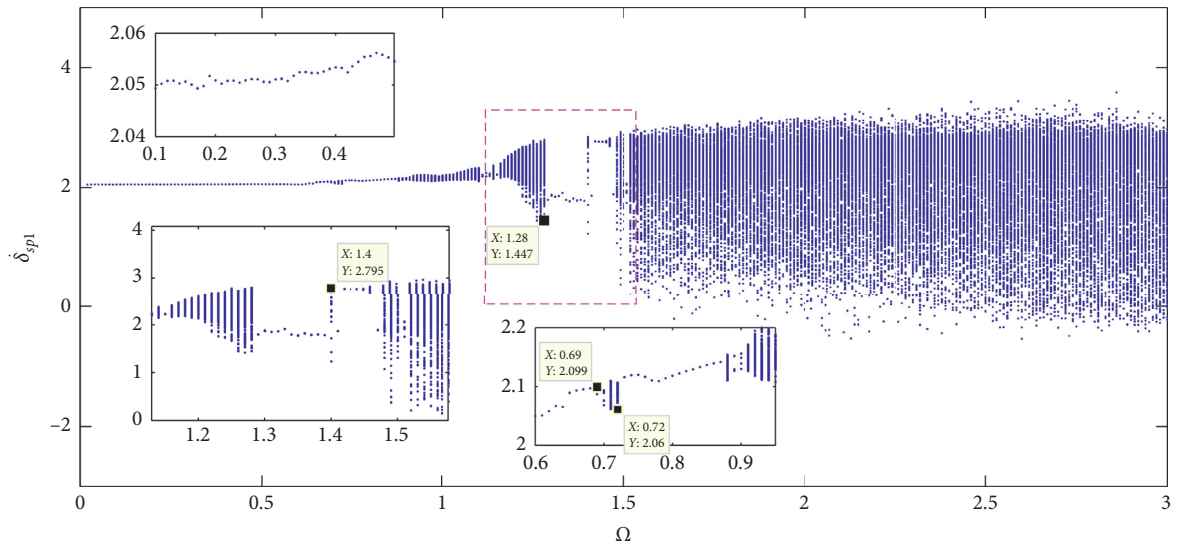

Figure 6: Bifurcation diagram of the health system with excitation frequency variation.

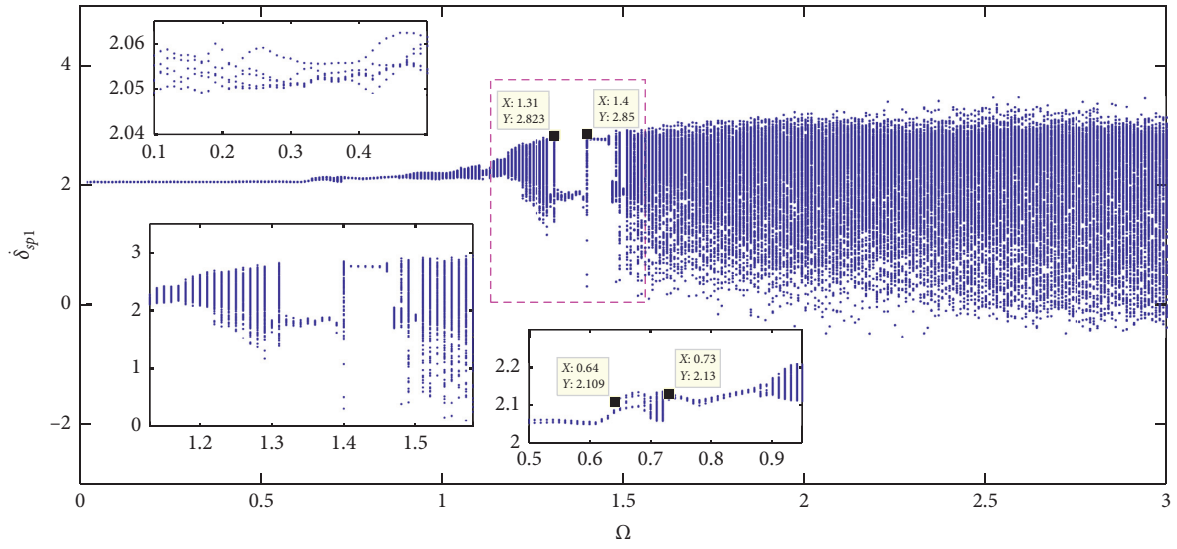

Figure 7: Bifurcation diagram of the fault system with excitation frequency variation.

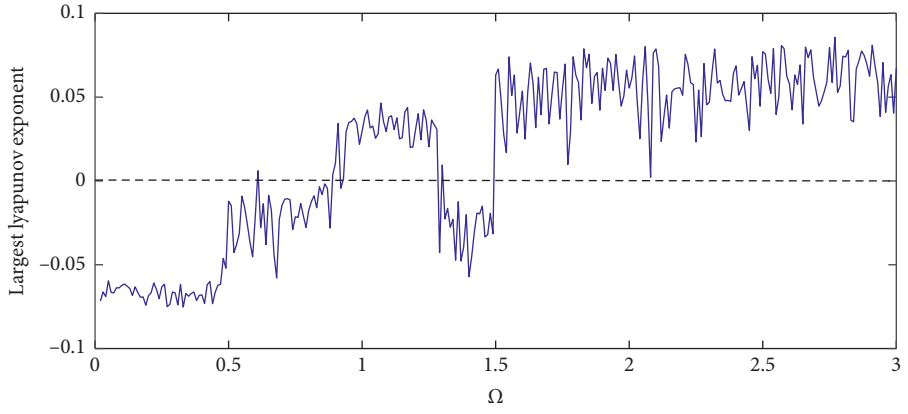

Figure 8: Largest Lyapunov exponent diagram of the health system with frequency variation.

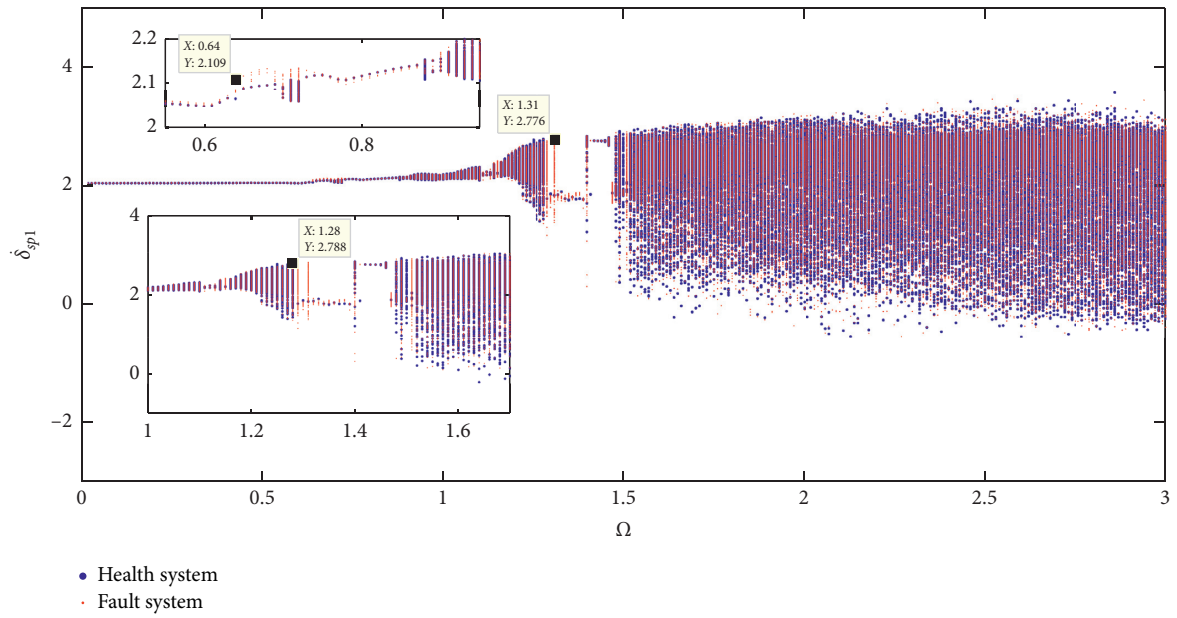

Figure 9: Bifurcation comparison diagram with frequency of the fault system and health system.

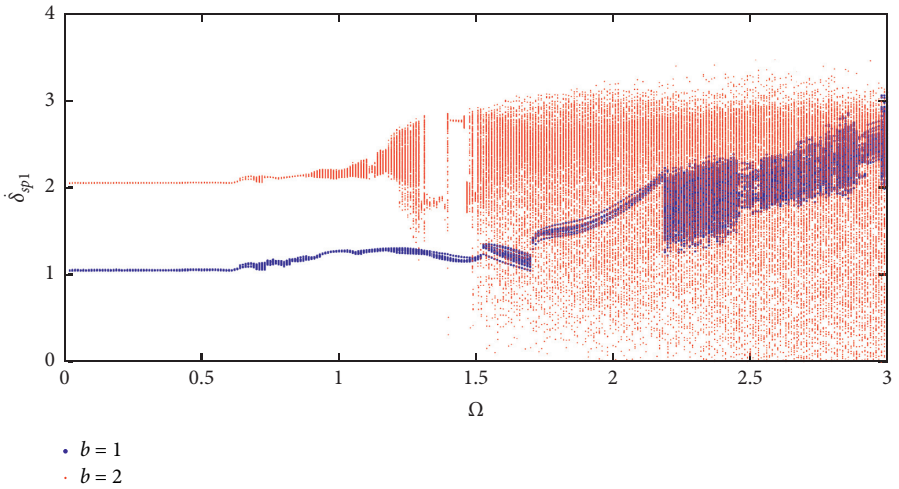

Figure 10: Bifurcation comparison diagram with frequency of the fault system and health system.

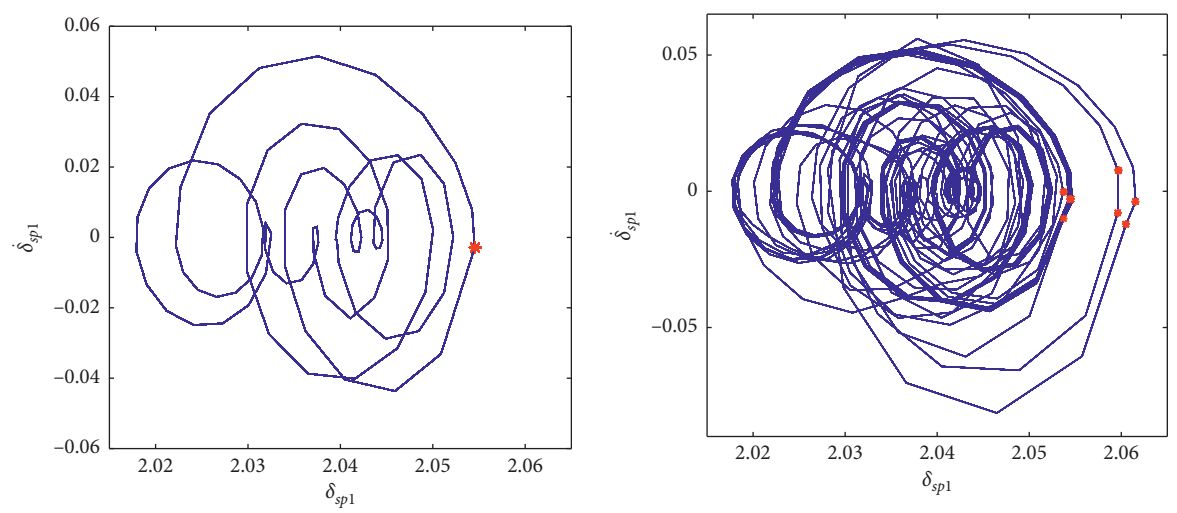

Figure 11: (a) Health system at Ω = 0.5. (b) Fault system at Ω = 0.5.

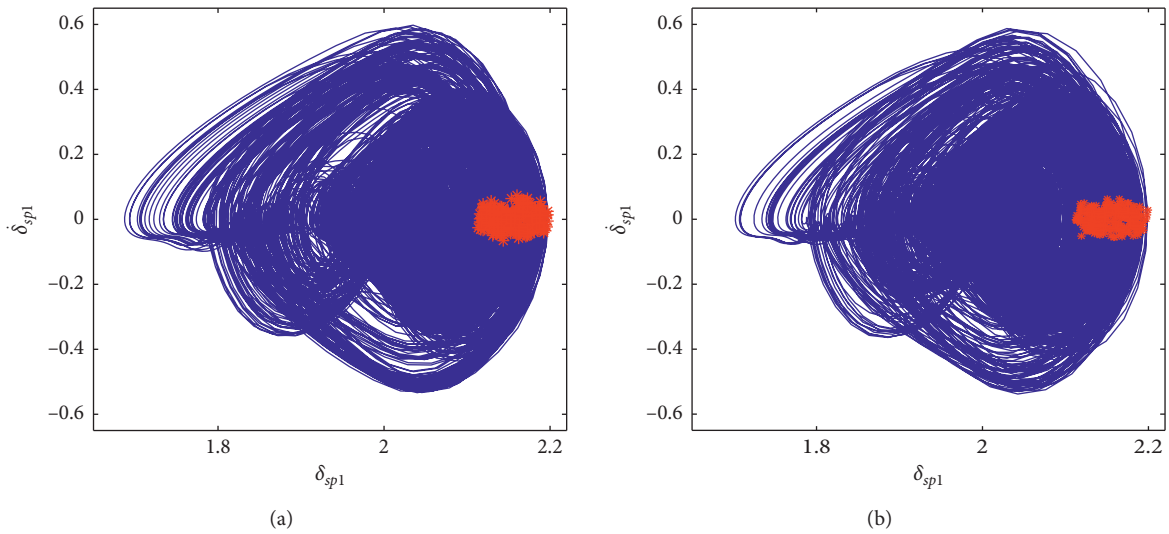

Figure 12: (a) Health system at $\Omega = 1$. (b) Fault system at $\Omega = 1$.

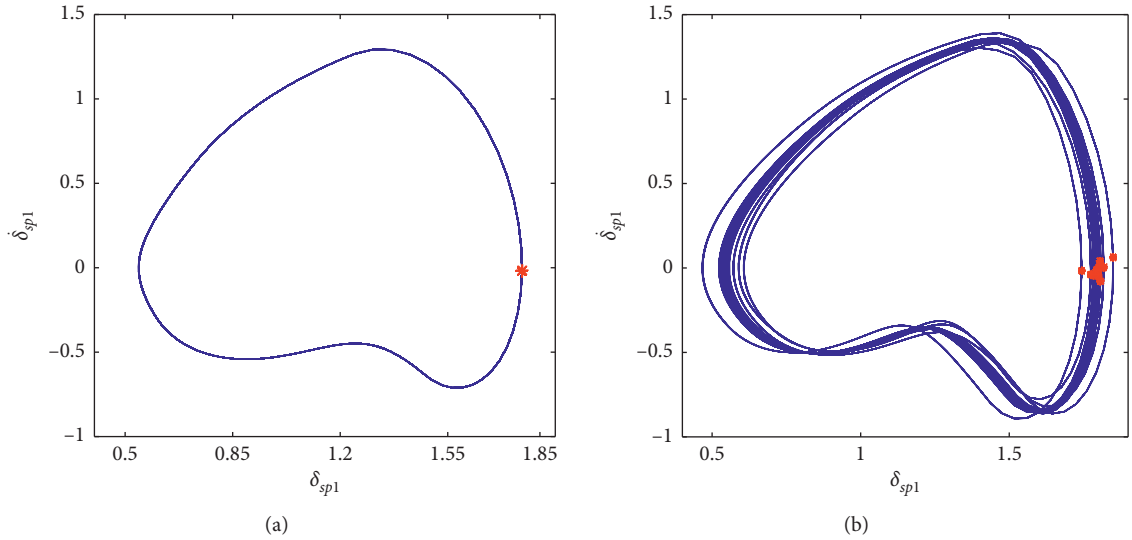

Figure 13: (a) Health system at $\Omega = 1.34$. (b) Fault system at $\Omega = 1.34$.

the health system and the fault system are shown in Figures 16 and 17, respectively. The largest Lyapunov exponent diagram of the health system is shown in Figure 18. It can be seen from the figures that the amplitude of the system motion augments with the increase of the backlash. For the health system, when the backlash b changes between 0 and 1.095, the system presents a single-period motion and the largest Lyapunov exponent is less than zero. However, the

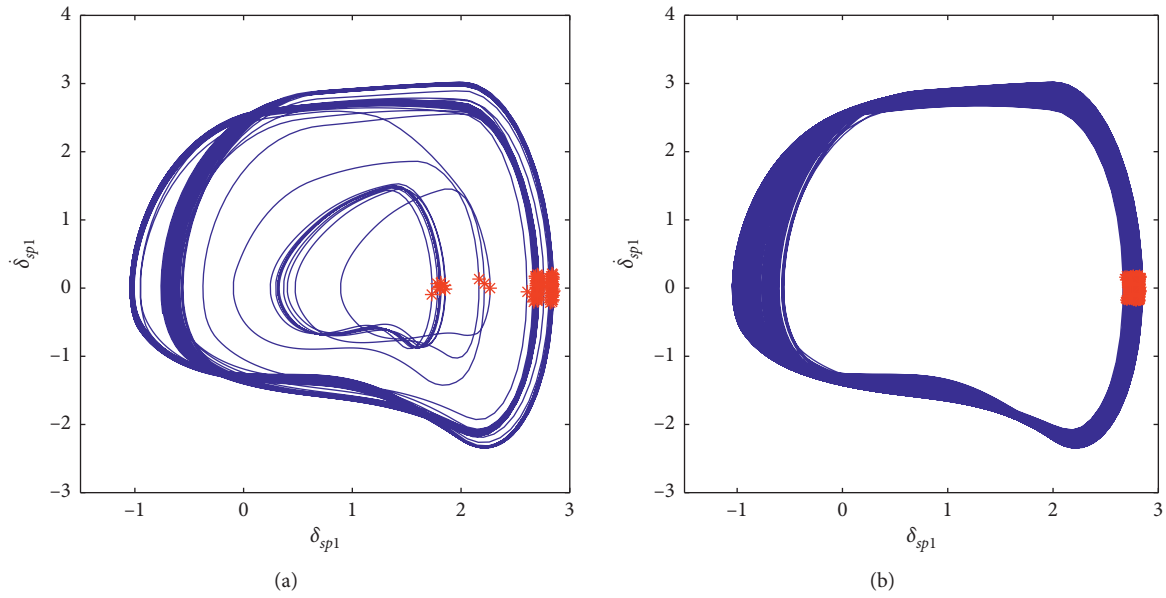

Figure 14: (a) Health system at $\Omega = 1.4$. (b) Fault system at $\Omega = 1.4$.

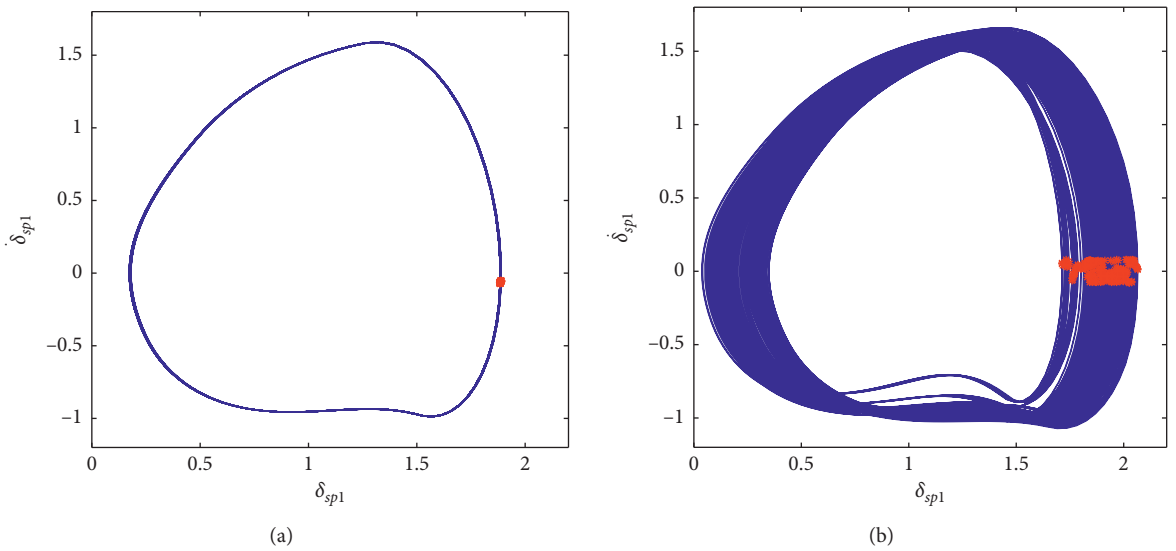

Figure 15: (a) Health system at $\Omega = 1.47$. (b) Fault system at $\Omega = 1.47$.

system motion state occurs jump variation at $b = 1.095$. Then, the system enters a small amplitude chaotic motion at the interval of 1.095–1.29 corresponding to which the largest Lyapunov exponent is larger than zero. Afterwards, the system reenters the single-period motion when b varies in 1.29–1.53. As b continues to increase, and the system eventually enters chaotic motion. For the fault system, it is similar to the state of motion experienced by the health system, but in the backlash interval corresponding to the periodic motion state of the health system, the fault system

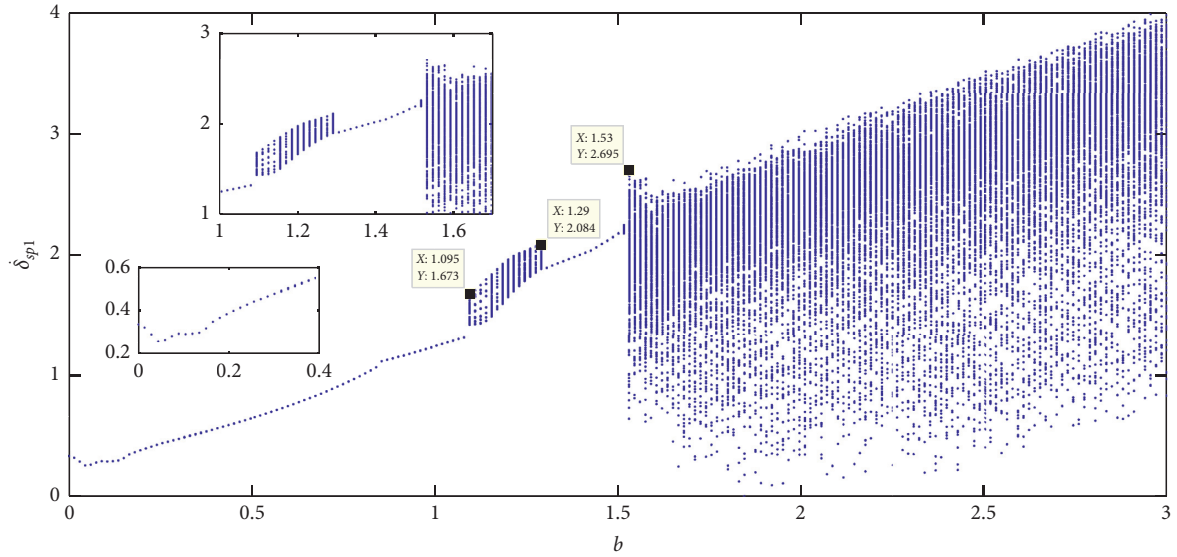

Figure 16: Bifurcation diagram of the health system with backlash variation.

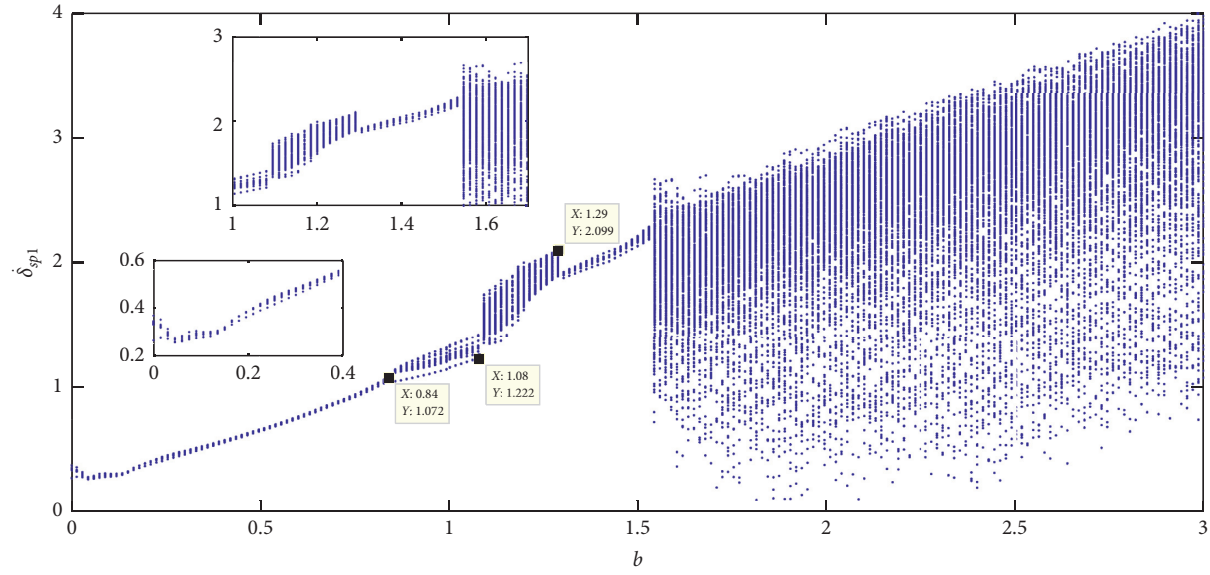

Figure 17: Bifurcation diagram of the fault system with backlash variation.

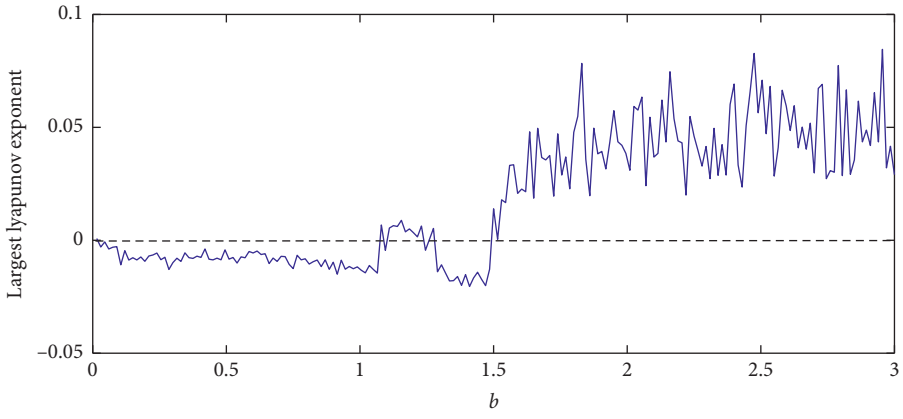

Figure 18: Largest Lyapunov exponent diagram of the health system with backlash variation.

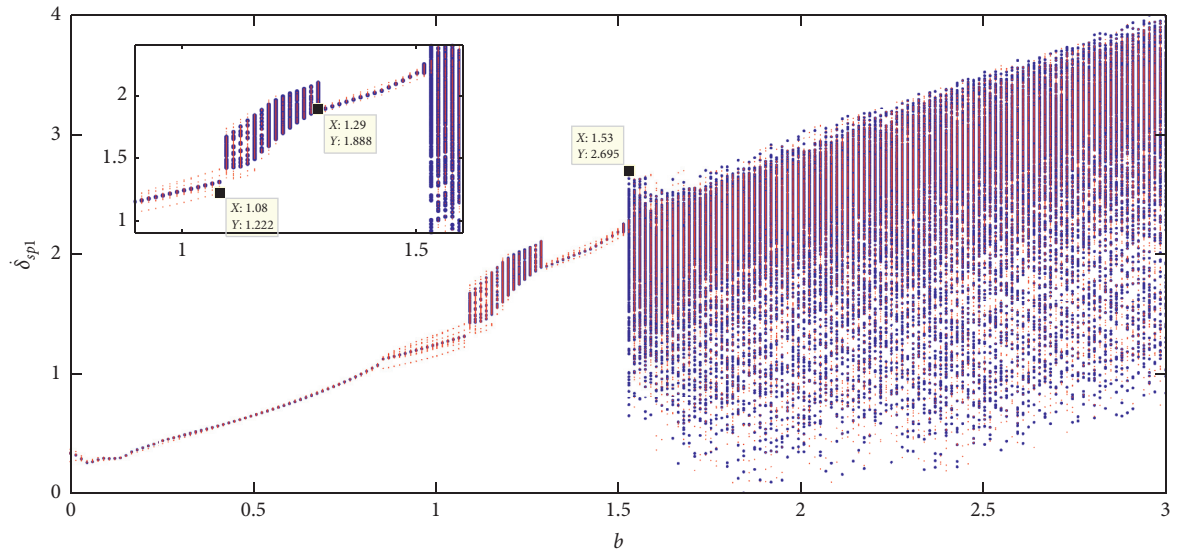

Figure 19: Bifurcation comparison diagram with backlash of the fault system and health system.

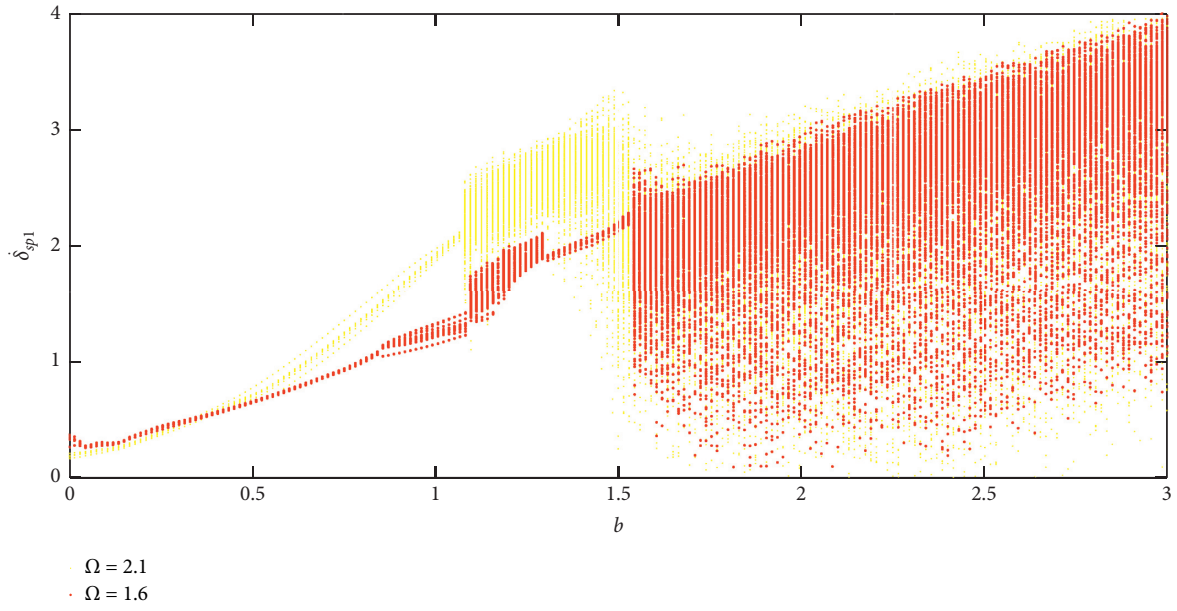

Figure 20: Bifurcation comparison diagram with backlash of the fault system and health system.

shows obvious small amplitude chaotic motion. Figure 19 shows the bifurcation characteristics of the two health systems with backlash. It can be seen from the figure that the fault system has more complex nonlinear characteristics and enters the chaotic motion earlier. After changing the speed, the bifurcation diagram of the fault system with the backlash is shown in Figure 20. When the speed increases, the amplitude of the chaotic motion will increase accordingly.

In order to further analyze the local characteristics of the health system and fault system and reveal the path of the

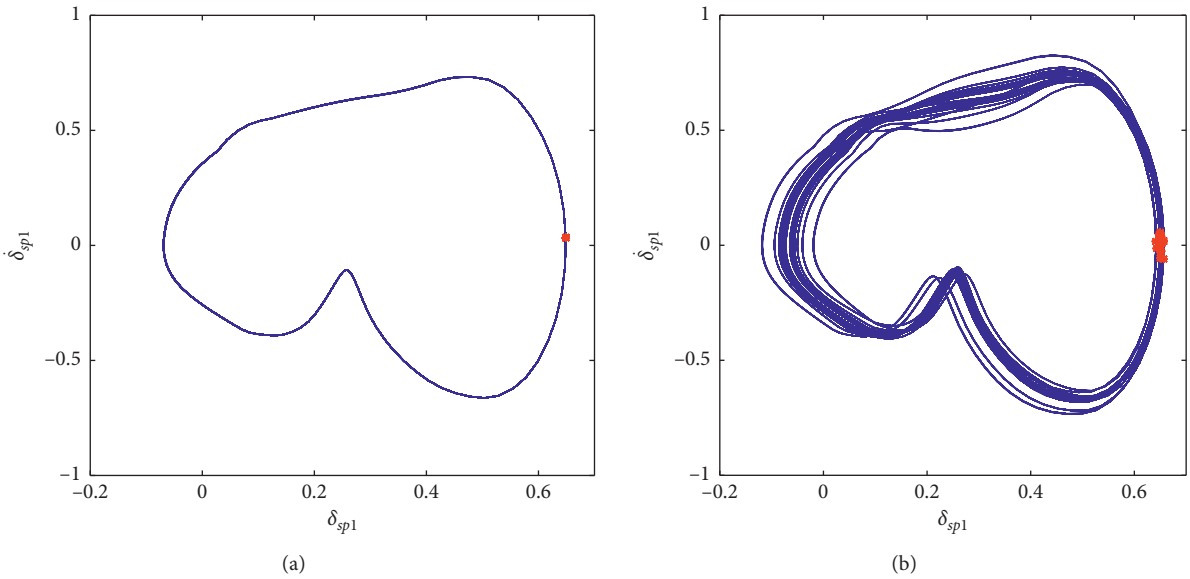

Figure 21: (a) Health system at $b = 0.5$. (b) Fault system at $b = 0.5$.

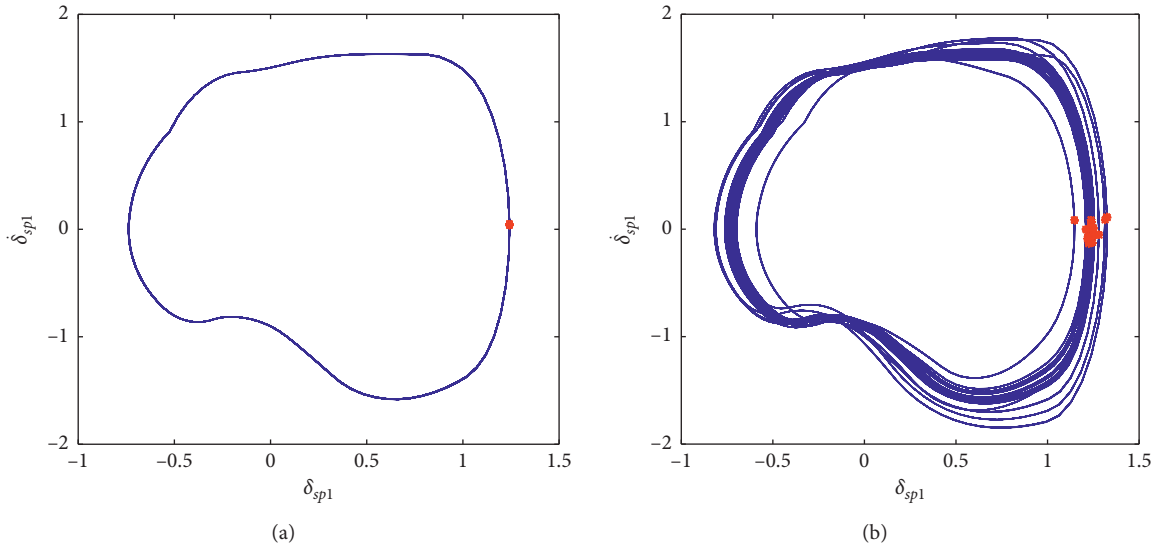

Figure 22: (a) Health system at $b = 1$. (b) Fault system at $b = 1$.

system into chaos, phase diagrams and Poincaré maps are used to describe the local characteristics of the system. From Figures 21–24, it can be seen that the health system exhibits a single-period motion at $b = 0.5$, 1, and 1.4 and a small amplitude chaotic motion at 1.2. While, the fault system directly enters the chaotic motion.

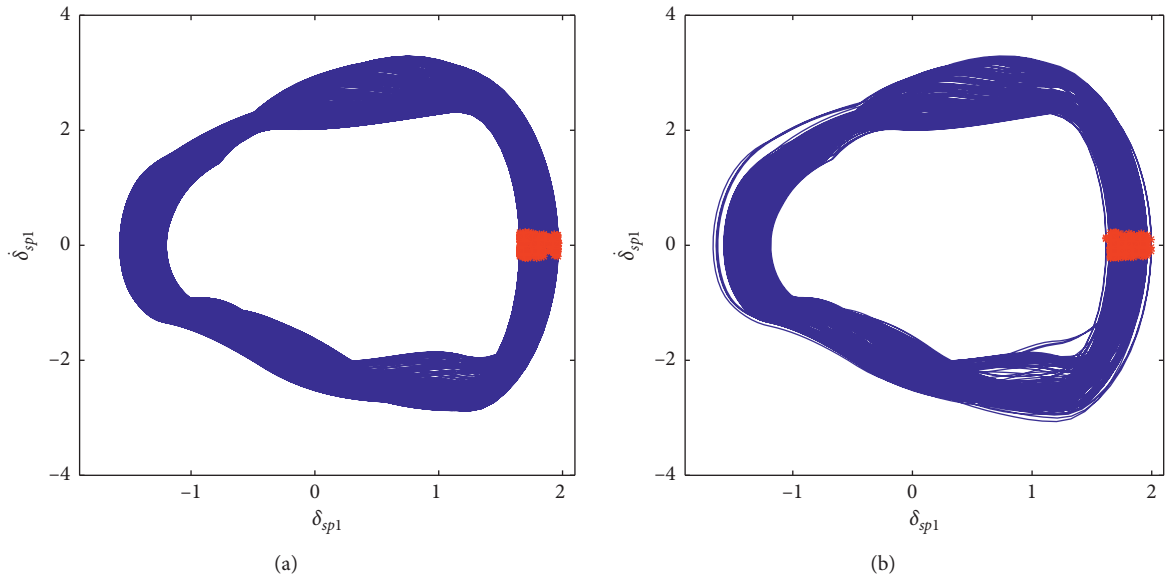

Figure 23: (a) Health system at $b = 1.2$. (b) Fault system at $b = 1.2$.

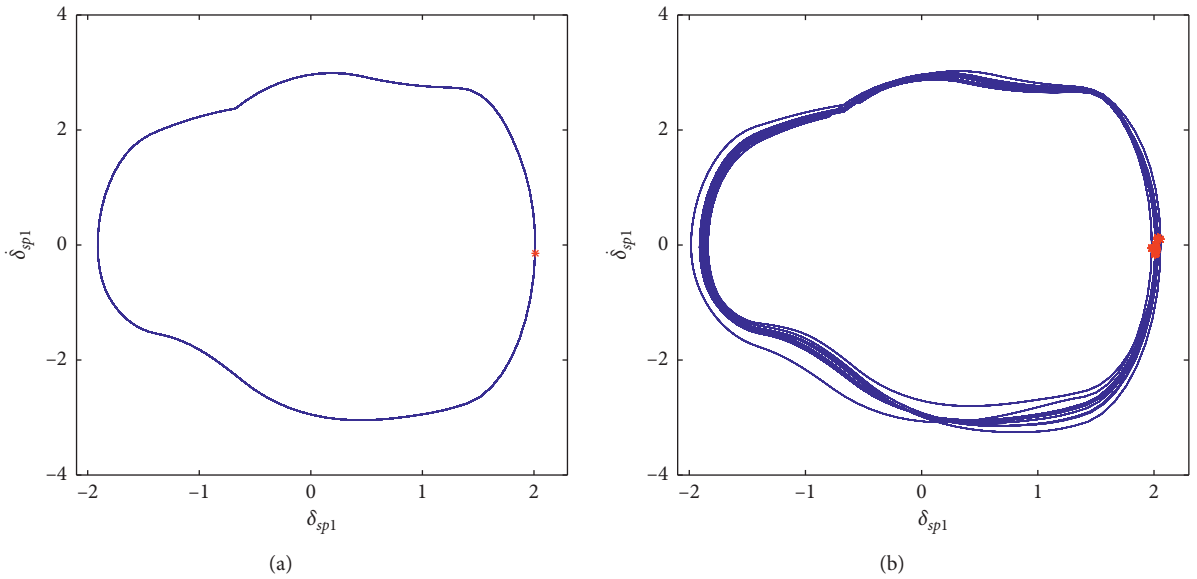

Figure 24: (a) Health system at $b = 1.4$. (b) Fault system at $b = 1.4$.

4. Conclusions

This study proposed a meshing stiffness model of gear pair with tooth tip chipping fault by combining the analytic geometry method and potential energy method. Then, a new nonlinear dynamic model of the planetary gear system under health and fault conditions is established considering the time-varying mesh stiffness, tooth backlash, and static transmission error. The model is derived by the Lagrangian method and solved by the numerical integration method. Taking the dynamic transmission error between the sun gear and planet gear as the research object, through the global bifurcation diagram, the variations of the two system motion states with the excitation frequency and tooth backlash are analyzed, and the local characteristics of the systems are analyzed via the phase diagrams and the Poincaré maps. Some conclusions can be obtained as follows:

(1) With the variation of excitation frequency, both the health system and fault system show complex bifurcation and chaotic characteristics, and the chaotic motion is mixed with periodic windows;

(2) The fault system has more complex nonlinear characteristics and enters the chaotic motion earlier. The fault system shows multiple periodic motions and a small amplitude chaotic motion in the interval

of excitation frequency and backlash, in which the health system is in the periodic motion state;

(3) The amplitude of the chaotic motion augments with the increase of the initial backlash. The system enters the chaotic motion earlier as the speed increases if the backlash is designed large;

(4) When the initial backlash of the design is determined, the amplitude of the chaotic motion will increase with the speed

Nomenclature

α_2: Central angle of half tooth
α_x: Pressure angle of involute point
θ_x: Evolving angle of involute point
R_b: Base circle radius
α_a: Pressure angle of point A
h_a^*: Addendum coefficient
m: Gear modulus
α_t: Addendum circle pressure angle
y_{xL_1}: y-coordinate of the intersection of cross-section and L_1
y_{xL_3}: y-coordinate of the intersection of cross-section and L_3
x_i: y_i $(i = a, b, c)$ coordinate of the points A, B, and C
α_0: Pitch circle pressure angle
α_t: Addendum pressure angle
z_e: Number of external gear teeth
I_x: Moment of inertia of tooth cross-section
d: Distance between action point and tooth root circle
h: Distance between action point and X-axis
h_x: Distance between arbitrary point on involute and X-axis
x: Distance of involute point to tooth root circle
L: Gear tooth width
A_x: Area of tooth cross-section
E: Elastic modulus
G: Shear modulus
v: Poisson ratio
z_{xL_2}: z-coordinate of the intersection of cross-section and L_2
α_1: Pressure angle of action point
ω_c: Angular frequency of the carrier
z_r: Tooth number of the ring gear
e_{aspn}, e_{rspn}: Amplitudes of static transmission errors
ψ_{spn}, ψ_{rpn}: Initial phases
ξ_{spn}, ξ_{rpn}: Damping ratios
δ_{spn}, δ_{rpn}: Dynamic transmission errors
b_{spn}, b_{rpn}: Initial backlash.

Data Availability

The datasets that support the findings of this study are included within the article.

Conflicts of Interest

The authors declare that they have no conflicts of interest.

Acknowledgments

This research was funded by the Natural Science Foundation of Hebei Province of China (E2019202132), Science and Technology on Space Intelligent Control Laboratory (6142208190308), and Innovation Foundation of CAST (CAST-2021-01-11). These supports are gratefully acknowledged.

References

[1] A. Kumar, C. P. Gandhi, Y. Zhou, R. Kumar, and J. Xiang, "Latest developments in gear defect diagnosis and prognosis: a review," *Measurement*, vol. 158, Article ID 107735, 2020.

[2] A. Kahraman, "Load sharing characteristics of planetary transmissions," *Mechanism and Machine Theory*, vol. 29, no. 8, pp. 1151–1165, 1994.

[3] R. G. Parker and X. Wu, "Vibration modes of planetary gears with unequally spaced planets and an elastic ring gear," *Journal of Sound and Vibration*, vol. 329, no. 11, pp. 2265–2275, 2010.

[4] D. R. Kiracofe and R. G. Parker, "Structured vibration modes of general compound planetary gear systems," in *Proceedings of the ASME International Design Engineering Technical Conferences & Computers and Information in Engineering Conference 2007*, vol. 7, pp. 511–526, Las Vegas, NV, USA, September 2008.

[5] A. Mbarek, A. Hammami, A. Fernandez Del Rincon, F. Chaari, F. Viadero Rueda, and M. Haddar, "Effect of load and meshing stiffness variation on modal properties of planetary gear," *Applied Acoustics*, vol. 147, pp. 32–43, 2019.

[6] V. K. Ambarisha and R. G. Parker, "Suppression of planet mode response in planetary gear dynamics through mesh phasing," *Journal of Vibration and Acoustics*, vol. 128, no. 2, pp. 133–142, 2006.

[7] M. B. Sánchez, M. Pleguezuelos, and J. I. Pedrero, "Approximate equations for the meshing stiffness and the load sharing ratio of spur gears including Hertzian effects," *Mechanism and Machine Theory*, vol. 109, pp. 231–249, 2017.

[8] S. Mo, Y. Zhang, Q. Wu, S. Matsumura, and H. Houjoh, "Load sharing behavior analysis method of wind turbine gearbox in consideration of multiple-errors," *Renewable Energy*, vol. 97, pp. 481–491, 2016.

[9] S. Li, "Effects of machining errors, assembly errors and tooth modifications on loading capacity, load-sharing ratio and transmission error of a pair of spur gears," *Mechanism and Machine Theory*, vol. 42, no. 6, pp. 698–726, 2007.

[10] J. Wang, G. He, J. Zhang, Y. Zhao, and Y. Yao, "Nonlinear dynamics analysis of the spur gear system for railway locomotive," *Mechanical Systems and Signal Processing*, vol. 85, pp. 41–55, 2017.

[11] Y. Shen, S. Yang, and X. Liu, "Nonlinear dynamics of a spur gear pair with time-varying stiffness and backlash based on incremental harmonic balance method," *International Journal of Mechanical Sciences*, vol. 48, no. 11, pp. 1256–1263, 2006.

[12] H. Zhai, C. Zhu, C. Song, H. Liu, and H. Bai, "Influences of carrier assembly errors on the dynamic characteristics for

wind turbine gearbox," *Mechanism and Machine Theory*, vol. 103, pp. 138–147, 2016.

[13] C. Xun, X. Long, and H. Hua, "Effects of random tooth profile errors on the dynamic behaviors of planetary gears," *Journal of Sound and Vibration*, vol. 415, pp. 91–110, 2018.

[14] B. Zhao, Y. Huangfu, H. Ma, Z. Zhao, and K. Wang, "The influence of the geometric eccentricity on the dynamic behaviors of helical gear systems," *Engineering Failure Analysis*, vol. 118, Article ID 104907, 2020.

[15] Y. Yang, L. Cao, H. Li, and Y. Dai, "Nonlinear dynamic response of a spur gear pair based on the modeling of periodic mesh stiffness and static transmission error," *Applied Mathematical Modelling*, vol. 72, pp. 444–469, 2019.

[16] C. I. Park, "Dynamic behavior of the spur gear system with time varying stiffness by gear positions in the backlash," *Journal of Mechanical Science and Technology*, vol. 34, no. 2, pp. 565–572, 2020.

[17] J. Margielewicz, D. Gąska, and G. Litak, "Modelling of the gear backlash," *Nonlinear Dynamics*, vol. 97, no. 1, pp. 355–368, 2019.

[18] J.-W. Lu, H. Chen, F.-L. Zeng, A. F. Vakakis, and L. A. Bergman, "Influence of system parameters on dynamic behavior of gear pair with stochastic backlash," *Meccanica*, vol. 49, no. 2, pp. 429–440, 2014.

[19] C. Gill-Jeong, "Numerical study on reducing the vibration of spur gear pairs with phasing," *Journal of Sound and Vibration*, vol. 329, pp. 3915–3927, 2010.

[20] S. Wei, Q. K. Han, X. J. Dong, Z. K. Peng, and F. L. Chu, "Dynamic response of a single-mesh gear system with periodic mesh stiffness and backlash nonlinearity under uncertainty," *Nonlinear Dynamics*, vol. 89, no. 1, pp. 49–60, 2017.

[21] J. Wang, J. Zhang, Z. Yao, X. Yang, R. Sun, and Y. Zhao, "Nonlinear characteristics of a multi-degree-of-freedom spur gear system with bending-torsional coupling vibration," *Mechanical Systems and Signal Processing*, vol. 121, pp. 810–827, 2019.

[22] C. Xie, L. Hua, X. Han, J. Lan, X. Wan, and X. Xiong, "Analytical formulas for gear body-induced tooth deflections of spur gears considering structure coupling effect," *International Journal of Mechanical Sciences*, vol. 148, pp. 174–190, 2018.

[23] K. Huang, Z. Cheng, Y. Xiong, G. Han, and L. Li, "Bifurcation and chaos analysis of a spur gear pair system with fractal gear backlash," *Chaos, Solitons Fractals*, vol. 142, Article ID 110387, 2020.

[24] J. Parra and C. M. Vicuña, "Two methods for modeling vibrations of planetary gearboxes including faults: comparison and validation," *Mechanical Systems and Signal Processing*, vol. 92, pp. 213–225, 2017.

[25] X. Liu, Y. Yang, and J. Zhang, "Resultant vibration signal model based fault diagnosis of a single stage planetary gear train with an incipient tooth crack on the sun gear," *Renewable Energy*, vol. 122, pp. 65–79, 2018.

[26] R. G. Parker and Y. Guo, "Dynamic analysis of planetary gears with bearing clearance," *Journal of Computational and Nonlinear Dynamics*, vol. 7, Article ID 041002, 2012.

[27] T. Eritenel and R. G. Parker, "Nonlinear vibration of gears with tooth surface modifications," *Journal of Vibration and Acoustics, ASME*, vol. 135, no. 5, Article ID 051005, 2013.

[28] M. Zhao and J. C. Ji, "Nonlinear torsional vibrations of a wind turbine gearbox," *Applied Mathematical Modelling*, vol. 39, no. 16, pp. 4928–4950, 2015.

[29] L. Xiang, N. Gao, and A. Hu, "Dynamic analysis of a planetary gear system with multiple nonlinear parameters," *Journal of Computational and Applied Mathematics*, vol. 327, pp. 325–340, 2018.

[30] J.-F. Shi, X.-F. Gou, and L.-Y. Zhu, "Modeling and analysis of a spur gear pair considering multi-state mesh with time-varying parameters and backlash," *Mechanism and Machine Theory*, vol. 134, pp. 582–603, 2019.

[31] W. Pan, X. Li, L. Wang, and Z. Yang, "Nonlinear response analysis of gear-shaft-bearing system considering tooth contact temperature and random excitations," *Applied Mathematical Modelling*, vol. 68, pp. 113–136, 2019.

[32] J. Liu, R. Pang, S. Ding, and X. Li, "Vibration analysis of a planetary gear with the flexible ring and planet bearing fault," *Measurement*, vol. 165, Article ID 108100, 2020.

[33] W. Luo, B. Qiao, Z. Shen, Z. Yang, H. Cao, and X. Chen, "Investigation on the influence of spalling defects on the dynamic performance of planetary gear sets with sliding friction," *Tribology International*, vol. 154, Article ID 106639, 2021.

[34] L. Xiang, C. An, Y. Zhang, and A. Hu, "Failure dynamic modelling and analysis of planetary gearbox considering gear tooth spalling," *Engineering Failure Analysis*, vol. 125, Article ID 105444, 2021.

[35] Z. Shen, B. Qiao, L. Yang, W. Luo, and Z. Yang, "Fault mechanism and dynamic modeling of planetary gear with gear wear," *Mechanism and Machine Theory*, vol. 155, Article ID 104098, 2021.

[36] Y. Yang, W. Xia, J. Han, Y. Song, J. Wang, and Y. Dai, "Vibration analysis for tooth crack detection in a spur gear system with clearance nonlinearity," *International Journal of Mechanical Sciences*, vol. 157-158, pp. 648–661, 2019.

[37] Z. G. Chen and Y. M. Shao, "Dynamic features of a planetary gear system with tooth crack under different sizes and inclination angles," *Journal of Vibration and Acoustics-Transactions of the ASME*, vol. 135, Article ID 031004, 2013.

[38] H. Z. Han, Z. F. Zhao, H. X. Tian, H. Ma, Y. Yang, and X. Li, "Fault feature analysis of planetary gear set influenced by cracked gear tooth and pass effect of the planet gears," *Engineering Failure Analysis*, vol. 121, Article ID 105162, 2021.

[39] F. Jiang, K. Ding, G. L. He, Y. L. Sun, and L. H. Wang, "Vibration fault features of planetary gear train with cracks under time-varying flexible transfer functions," *Mechanism and Machine Theory*, vol. 158, Article ID 104237, 2021.

[40] Y. Luo, N. Baddour, and M. Liang, "Dynamical modeling and experimental validation for tooth pitting and spalling in spur gears," *Mechanical Systems and Signal Processing*, vol. 119, pp. 155–181, 2018.

[41] Z. G. Chen, Z. W. Zhou, W. M. Zhai, and K. Y. Wang, "Improved analytical calculation model of spur gear mesh excitations with tooth profile deviations," *Mechanism and Machine Theory*, vol. 149, Article ID 103838, 2020.

[42] H. Ma, R. Song, X. Pang, and B. Wen, "Time-varying mesh stiffness calculation of cracked spur gears," *Engineering Failure Analysis*, vol. 44, pp. 179–194, 2014.